



Changes in the pore network structure of Hanford sediment after reaction with caustic tank wastes

L.E. Crandell^a, C.A. Peters^{a,*}, W. Um^b, K.W. Jones^c, W.B. Lindquist^d

^a Princeton University, Princeton, New Jersey, USA

^b Pacific Northwest National Laboratory, Richland, WA, USA

^c Brookhaven National Laboratory, Upton, NY, USA

^d Stony Brook University, Stony Brook, NY, USA

ARTICLE INFO

Article history:

Received 3 October 2011

Received in revised form 30 January 2012

Accepted 1 February 2012

Available online 9 February 2012

Keywords:

Mineral precipitation

Porosity

SEM

Pore size distribution

Erosion dilation

ABSTRACT

At the former nuclear weapon production site in Hanford, WA, caustic radioactive tank waste leaks into subsurface sediments and causes dissolution of quartz and aluminosilicate minerals, and precipitation of sodalite and cancrinite. This work examines changes in pore structure due to these reactions in a previously-conducted column experiment. The column was sectioned and 2D images of the pore space were generated using backscattered electron microscopy and energy dispersive X-ray spectroscopy. A pre-precipitation scenario was created by digitally removing mineral matter identified as secondary precipitates. Porosity, determined by segmenting the images to distinguish pore space from mineral matter, was up to 0.11 less after reaction. Erosion–dilation analysis was used to compute pore and throat size distributions. Images with precipitation had more small and fewer large pores. Precipitation decreased throat sizes and the abundance of large throats. These findings agree with previous findings based on 3D X-ray CMT imaging, observing decreased porosity, clogging of small throats, and little change in large throats. However, 2D imaging found an increase in small pores, mainly in intra-granular regions or below the resolution of the 3D images. Also, an increase in large pores observed via 3D imaging was not observed in the 2D analysis. Changes in flow conducting throats that are the key permeability-controlling features were observed in both methods.

© 2012 Elsevier B.V. All rights reserved.

1. Introduction

In subsurface sediments, mineral dissolution and precipitation reactions alter porosity and pore and throat size distributions, and these changes in the pore network can change the flow permeability and paths of the medium (Cai et al., 2009; Colon et al., 2004; Emmanuel and Berkowitz, 2005; Um et al., 2005). While dissolution increases porosity and permeability, effects of precipitation are much less understood (Gouze et al., 2001; Tenthorey and Scholz, 2002). Precipitation can occur both on grain surfaces and between grains,

cementing them together (Bickmore et al., 2001). This may alter flow paths, decrease permeability, and affect pore size distributions both by decreasing pore sizes and by creating small pores in the newly formed minerals (Aharonov et al., 1998). Beyond altering permeability, pore sizes impact geochemical reactions in other important ways. Pore sizes directly affect dissolution and precipitation rates by controlling available surface area (Lasaga, 1998). Additionally, it has been shown that mineral solubility and the impact of crystallization pressure varies with pore size (Emmanuel and Berkowitz, 2007; Rijniers et al., 2005; Scherer, 2004).

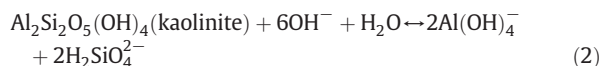
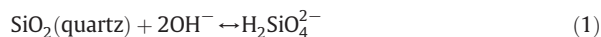
Despite advances in our understanding of geochemical reactions, it is still unknown where, within a single pore and a network of pores, precipitation will preferentially occur. Tenthorey and Scholz (2002) found that dissolution of quartz and labradorite resulted in secondary mineral precipitation

* Corresponding author at: Department of Civil & Environmental Engineering, Princeton University, Princeton, NJ 08544, USA. Tel.: +1 609 258 5645; fax: +1 609 258 2799.

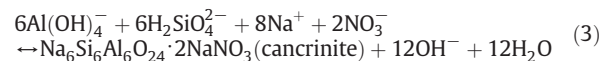
E-mail address: cap@princeton.edu (C.A. Peters).

in narrow pore throats and in areas with fine-grained material which provided a greater surface area for reaction and transient reaction kinetics. Conversely, Emmanuel et al. (2010) found precipitation to be suppressed in small pores (less than 10 μm in diameter) due to interfacial energy effects which increased solubility in small pores and instead found precipitation in large pores.

In this study, the effect of precipitation on pore and throat size distributions in the context of the Hanford, WA site is examined. The Hanford, WA site is a former nuclear weapon production plant where high-level nuclear waste was stored underground in 177 tanks, 67 of which have been leaking into the vadose zone sediments (Qafoku et al., 2003). This tank waste is highly caustic (pH 8 to 14), high temperature (60–110 $^{\circ}\text{C}$), high ionic strength (2–16 M NaNO_3), and has a high concentration of dissolved aluminum (0.7 to 2 M) (Kaplan et al., 2000; Liu et al., 2003; McKinley et al., 2001; Zachara et al., 2002). Additionally, the wastes contain a variety of radionuclides such as ^{90}Sr , ^{137}Cs , ^{238}U , and ^{129}I . The caustic nature of the waste causes dissolution of quartz and primary silicate minerals, e.g.



(Deng et al., 2006). Secondary precipitates, zeolite Linde Type A (LTA), sodalite and cancrinite, form from further reaction with sodium and nitrate, e.g.



(Deng et al., 2006). They have been experimentally shown to nucleate on and cement together quartz grains (Bickmore et al., 2001). These secondary precipitates are zeolite-like minerals with cage structures capable of taking up large radionuclides such as Cs and Sr (Chang et al., 2011; Chorover et al., 2003; Mon et al., 2005; Rod et al., 2010).

Flow-through column experiments reacting Hanford sediments with simulated caustic tank waste performed at PNNL have shown that mineral dissolution and precipitation alter the structure of the pore space (Cai et al., 2009; Um et al., 2005). 3D X-ray computed micro-tomography (CMT) was used to scan the column before and after the reactive flow experiment to provide a qualitative interpretation of changes in the pore structure (Um et al., 2005). Cai et al. (2009) replicated this experiment and used 3D CMT to track changes in the pore structure by scanning before, during, and after reaction. It was concluded that precipitation and dissolution reactions were responsible for decreasing porosity as well as the total number of pores and throats. A shift in the pore and throat size distributions was observed that included a loss in small pores and throats and an increase in the number of large pores.

Tracking reaction-induced changes in pore and throat size distributions is the first step in predicting corresponding changes in system permeability. A shift in throat size distribution that decreases the size of all throats would be

indicative of a decrease in system permeability. A throat size distribution that decreases the number of small throats and increases the number of large throats may reflect the creation of preferential flow paths and no change or even an increase in permeability. While throat sizes are the most important for determining permeability, changes in the sizes of pores can provide information on where, within a network of pores, precipitation occurs. A decrease in all pore sizes suggests that precipitation is independent of pore size. If this occurs with no change in throat size distribution, porosity is expected to decrease without a change in permeability. Changes in fluid transport properties of a system can be estimated by creating pore network models using the pore and throat size distributions as input (Algive et al., 2010; Van Marcke et al., 2010; Vogel and Roth, 2001). Vogel and Roth (2001) found the relative hydraulic conductivity of a soil calculated from a network model based on measured pore geometries and a connectivity function based on the 3D Euler number to agree relatively well with measured values. Van Marcke et al. (2010) created a pore network model based on X-ray CT determined pore sizes and calculated permeability by applying a finite difference computational fluid dynamics (CFD) method to simulate flow in the network. They found good agreement between permeabilities determined using traditional computationally intensive CFD approaches and their pore network model approach (Van Marcke et al., 2010).

In this study, the reacted column detailed in Cai et al. (2009), “column X”, was sectioned and examined using 2D scanning electron microscopy (SEM). The need for sectioning limits the number of images that can be obtained, but SEM imaging produces higher resolution images than CMT imaging. Furthermore, the ability to do backscattered electron (BSE) and energy-dispersive X-ray spectroscopy (EDS) enables determination of mineralogical detail. One objective of this study was to use SEM imaging to analyze precipitation-induced changes in pore network structure. Additionally, the capability of SEM imaging to provide information on pore network structures beyond that which can be obtained from 3D imaging was assessed. This was achieved by computing pore and throat size distributions for three cross sections of the column using an erosion–dilation analysis. These distributions are compared with the pre-precipitation scenario created by digitally removing precipitation from the cross sectional BSE images. Loose grains from column X were also imaged and compared to unreacted Hanford sediment grains to identify the morphology of secondary precipitates forming on grain surfaces.

2. Methods

2.1. Column sectioning

Column X is a 3.1 mm ID \times 8.8 cm PEEK column. This column had been packed with 200–300 μm diameter Hanford sediment and reacted with simulated tank waste (2 M NaNO_3 , 1.2 M NaOH , and 0.05 M $\text{Al}(\text{NO}_3)_3$) (Cai et al., 2009). After the reactive flow experiment and 3D CMT scanning had been finished, the column was shipped to Princeton for SEM imaging. Column X was flushed with ethanol (200 proof, ACS/USP grade) then dried with desiccated air. This

was followed by flowing Epo-Thin epoxy (Buehler, Lake Bluff, IL) through the column using a combination of pressure-induced flow and vacuum applied at the column outlet. Epo-Thin was selected because of its low viscosity, low shrinkage, and slow curing time. This method was successful in advancing epoxy into 3 cm of the column before the back-pressure became prohibitive for further flow. The column was then shipped to Applied Petrographic Services, Inc. (Greensburg, PA) to be sectioned, polished, and coated for SEM imaging. The column was sectioned at three places, identified as “X2”, “X3”, and “X4” at approximately 2.2, 1.6, and 1.2 cm from the inlet respectively.

2.2. SEM imaging

SEM imaging of the polished cross sections was performed using the FEI Quanta 200 FEG Environmental SEM at the Princeton PRISM Imaging and Analysis Center (IAC). BSE imaging as well as EDS imaging was performed to identify minerals. Sodalite and cancrinite precipitates were identified based on morphological features given in Barnes et al. (1999), Bickmore et al. (2001), Buhl et al. (2000), and Um et al. (2005) and confirmed by elemental information from EDS analysis. For each section, X2, X3 and X4, a composite image up to 3.4 by 3.4 mm was generated from up to 26 high-resolution BSE images, maintaining a resolution of 0.4 μm .

In addition to the SEM imaging of polished sections, loose grains of the reacted sediments were examined. Grains were removed from the end of column X and adhered to carbon tape. These were imaged using BSE and EDS images in low vacuum mode on the environmental SEM. This was done to assess the distribution of clay and secondary mineral coatings on grain surfaces. Additionally, this allowed examination of precipitate

mineral morphologies, and comparison with the previous studies.

2.3. Pore space analysis

The composite grayscale BSE images were segmented to create a binary image of pore space and mineral matter. This was done manually in Adobe Photoshop™ through a repetitive process of adjusting grayscale intensities to enhance the spread of mid-level intensities and visually assessing thresholds on a grain-by-grain basis. These segmented composite images were used to calculate pore and throat size distributions at sections X2, X3 and X4 using an erosion and dilation method as introduced in seminal work by Doyen (1988) and Ehrlich et al. (1984). In this method, pore sizes are defined by the size of the largest circle that fits entirely within the pore element. Pore sizes are determined by eroding pore elements using a circular structuring element that increases in radius by 1 pixel (0.4 μm) every cycle. In a given cycle, the pore elements that disappear are counted and the pore size is noted by the size of the structuring element in that cycle. Fig. 1 shows the evolution of the pore space as the structuring element is increased in size. Pore seeds remaining in each image represent locations of pores that are greater in size than the current structuring element size. Fig. 1 shows the images from the erosion–dilation cycles up to a structuring element with a radius of 50 pixels (20 μm), but the process is continued until the last, largest, pores have disappeared. From the enumeration of pores at each size, the pore size distribution is determined. In this process, large connected pore space areas are separated into collections of smaller pores and throats. A pore throat is defined during a cycle when a pore area is separated into two smaller pores. This can be observed in Fig. 1 by noting how large pore areas

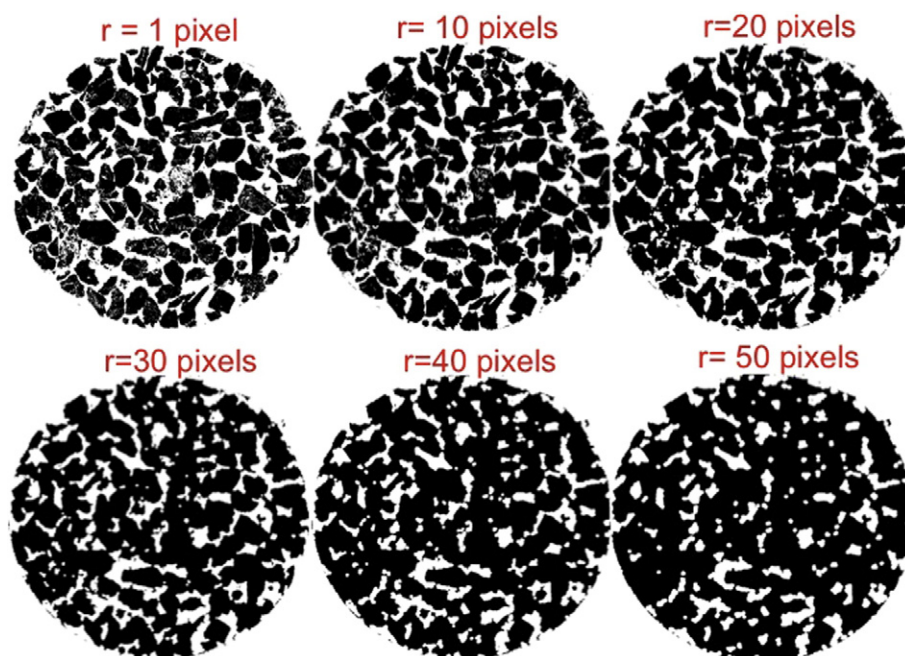


Fig. 1. Evolution of pore space during image erosion–dilation analysis with radial structuring element. Pores remaining in a given image indicate the location of a pore larger than the applied structuring element. In these images, 1 pixel equals 0.4 μm , and the circle diameter is 3.1 mm.

are broken into smaller pores as the structuring element size increases. The throat size distribution is determined by counting the number of throats defined during each cycle.

2.4. Bias correction

Two-dimensional analysis of pore and throat sizes has an inherent bias as a 2D cross section does not cut through the largest sections of all the pores and throats. Based on stereology theory, Weibel (1979) computed the bias correction value for a 2D interpretation of a random pack of 3D spheres. The mean radius measured in a 2D slice, \bar{r}_{2D} , is linearly related to the 3D structure by a constant, k

$$\bar{r}_{2D} = k r_{3D} \quad (4)$$

where r_{3D} is the radius of the spheres. For a random pack of 3D spherical objects of the same size, the theoretical value of k is $\pi/4$ (Weibel, 1979). For this work, in which the pores are not all of the same size, an empirical k value for the mean pore size, of radius \bar{r}_{3D} , in the column was estimated. The mean radius for the 3D pore elements was determined from the pore size distributions reported in Cai et al.

(2009). The mean radius for the 2D pore elements was determined from a set of BSE images processed to match 2D CMT images (previously obtained) in total pore space. A comparable set of 2D BSE images, which mimic the 2D CMT slices, was needed because the 2D SEM images capture intragranular pore space and small pores below the resolution level of CMT images that are thus not present in the 3D pore size distribution. This was achieved by processing the segmented BSE images to remove intragranular pores and small pores. These images matched the 2D CMT sections in terms of porosity and were used to find the mean radius for the 2D pores from the same erosion–dilation method described in Section 2.3. The progression of steps used to calculate the bias correction is shown in Fig. 2. Once the mean pore radius was determined for 3D and 2D data, the bias correction constant was calculated and used to correct pore size distributions from the original 2D segmented BSE images. This method is approximate as it assumes that the bias correction value for each pore size is equal to the value estimated for the mean pore size. The correction constant, k , for column X was found to be 0.437. Calculating this bias correction value for the column facilitates the use of higher resolution 2D SEM data to analyze the pore space without the drawbacks of underestimating pore and throat sizes.

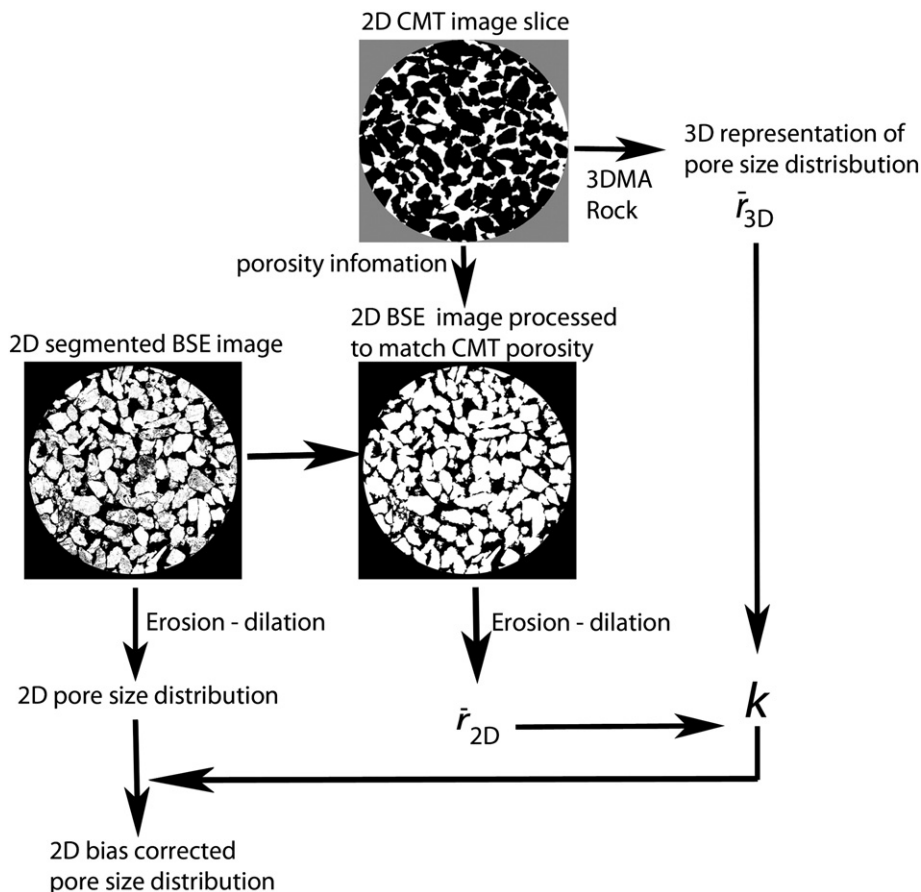


Fig. 2. Process used to determine empirical bias correction value, k , for 2D representation of pore sizes. Correction factor calculated from mean radii determined from 3D representation of pores and modified 2D BSE representation. Pore space is shown in white in the CMT slice and black in the BSE images.

2.5. Digital removal of precipitation

The post-reaction SEM imaging and analysis of column X allow for characterization of the final pore network structure, with newly formed precipitates in place. Ideally, one would be able to determine the impact of precipitation on the pore space, but to do this it is necessary to compare the post-reaction scenario to an initial scenario. Unfortunately, SEM imaging requires destructively sampling the column to prepare cross sections for analysis, which does not allow for an initial pre-reaction case to be imaged. As an approximation of the pre-reacted case, a set of images was created by digitally removing the precipitation.

Precipitates on grain surfaces and in intragranular pore regions were identified morphologically and confirmed using EDS analysis as a training set. Adobe Photoshop™ was then used to digitally remove precipitation in the cross sections based on the training analysis. This method is depicted in Fig. 3. Fig. 3a shows a portion of a BSE cross-section image depicting precipitation coating grain surfaces. Based on the described training, the precipitate was identified, as in Fig. 3b, and digitally removed to yield a pre-precipitation scenario, Fig. 3c. Despite every effort to be accurate and precise in this procedure, there is some error introduced from the occasional difficulty distinguishing secondary precipitates. This error is minimal on the grain surfaces, where secondary precipitates were more easily distinguishable, and more likely in small intragranular pores. In total, the error is likely to be small as the majority of precipitation, over 90%, occurred on grain surfaces.

A composite image for each of the three sections, X2, X3, and X4, was digitally altered to create the pre-precipitation composite images. The composite images were segmented using the same procedure described in Section 2.3. These were then analyzed using the erosion–dilation method to calculate pore and throat size distributions representative of the pre-reaction condition. It should be noted that this method of digitally removing precipitation produces only an approximation of the pre-reaction condition. Because reaction with caustic tank wastes also causes dissolution of quartz (and other primary minerals) that cannot be accounted for, this method may overestimate the initial pore space.

3. Results and discussion

3.1. SEM images of reacted samples

3.1.1. Precipitate morphology

SEM imaging of loose reacted Hanford sediment grains showed secondary mineral precipitates on grain surfaces with two different morphologies (Fig. 4). In some areas, secondary minerals had a ball-shaped morphology, consistent with cancrinite precipitation shown in previous studies (Bickmore et al., 2001; Um et al., 2005). In other areas, grain surfaces were covered with smooth amorphous secondary precipitates. Previous imaging work by Um et al. (2005) observed two morphologies of secondary mineral precipitates, aggregates of ball-shaped cancrinite and a smooth gel forming on mineral surfaces. They identified the amorphous gel as an amorphous aluminosilicate phase.

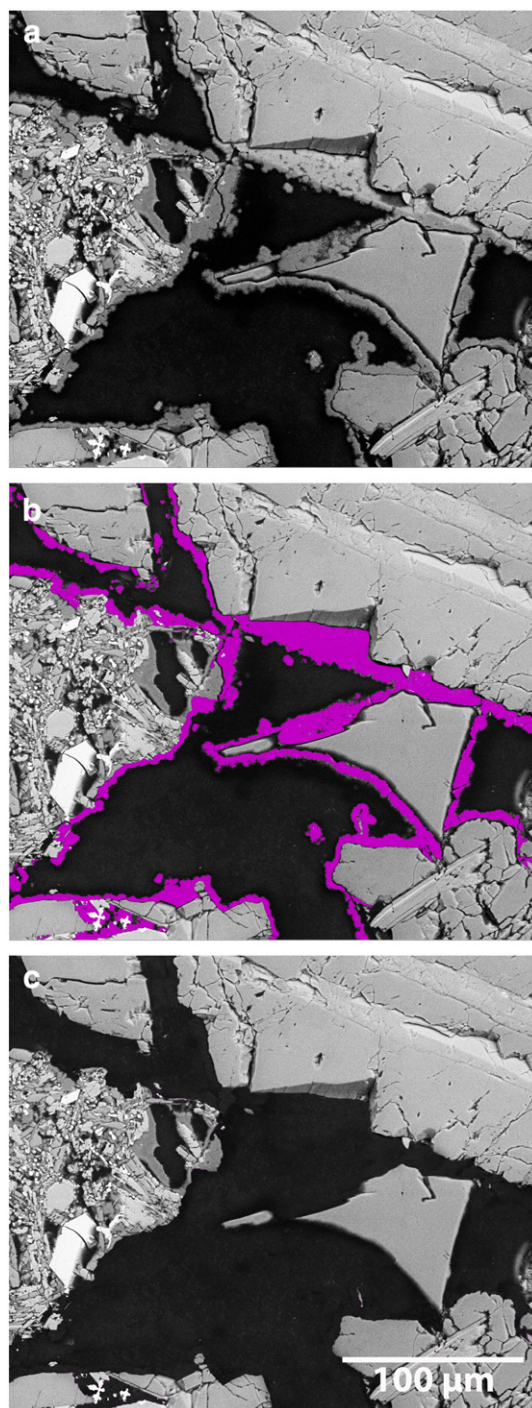


Fig. 3. Sample cross section BSE image showing sample with (a) precipitation present, (b) precipitation highlighted, and (c) precipitation digitally removed.

In this study, and in Um et al. (2005), ball-shaped cancrinite precipitation was observed on a smoother amorphous phase formed on grain surfaces as shown in Fig. 5. Finding cancrinite on the amorphous phase suggests this precipitate layer is a precursor for formation of ball-shaped aggregates of cancrinite. Cancrinite may nucleate on the surface and use it as a source for aluminum, sodium, and/or silica. Experimental

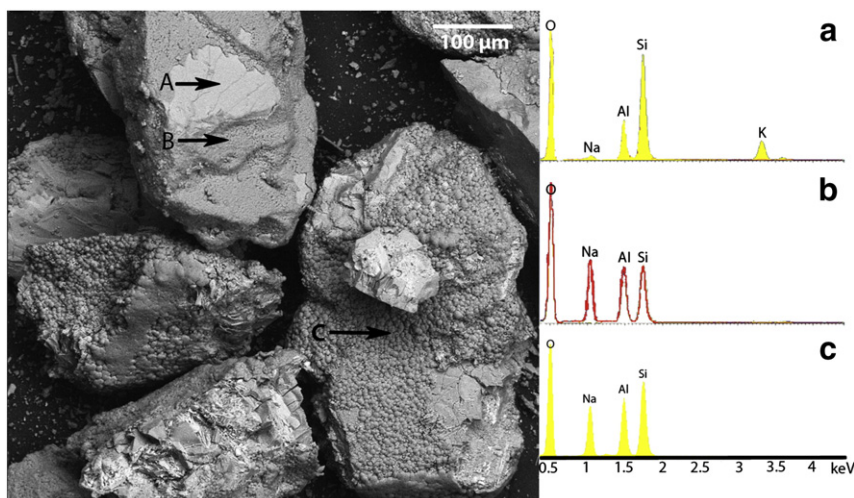


Fig. 4. BSE image of sodalite/cancrinite precipitation on reacted Hanford sand grains. Spectrum a shows K-feldspar grain with spectrum b reflecting the composition of the smoother morphology of sodalite/cancrinite precipitates on the grain surface. Shown in spectrum c is the composition of the ball-shaped morphology of cancrinite.

reaction of kaolinite with simulated tank waste leachate performed by [Crosson et al. \(2006\)](#) found that formation of sodalite and cancrinite was preceded by formation of one or more less crystalline Al-containing phases ([Crosson et al., 2006](#)). They suggest that cancrinite occurs as a secondary nucleation process at the expense of sodalite or another phase such as less crystalline-Al ([Crosson et al., 2006](#)).

SEM imaging reveals physical space between the precipitated amorphous phase and the grain surface ([Fig. 5](#)) suggesting that the secondary precipitate is not chemically bonded to the grain surface. A lack of strong chemical bonding of the secondary minerals to the grain surfaces at the Hanford site could lead to the transport of clusters of cancrinite precipitates downstream resulting in clogging and flow path alterations. Later, this issue is discussed again in the context of precipitate decohesion observed in the analysis of 2D cross sections.

3.1.2. Precipitate identification and distribution in 2D cross sections

Examination of the BSE images of cross sections from column X showed secondary mineral precipitation on grain surfaces and in pore throats ([Fig. 6](#)). EDS analysis confirmed dominant mineralogy of Na, Al, and Si, consistent with major elements of sodalite and cancrinite precipitation. Precipitation was evident on all grain surfaces as a relatively uniform coating ([Fig. 6](#)) suggesting no relationship to pore sizes, throat sizes, or mineralogy. The ball shaped morphology of cancrinite precipitates noted in [Section 3.1.1](#) is evident in these images as well. This morphology creates small pores in the newly formed minerals that are more easily observed in the cross sectional images ([Fig. 6](#)).

As mentioned in [Section 3.1.1](#), physical space between secondary precipitates and the grain surface was noted in SEM imaging of reacted grains. Further evidence of this was

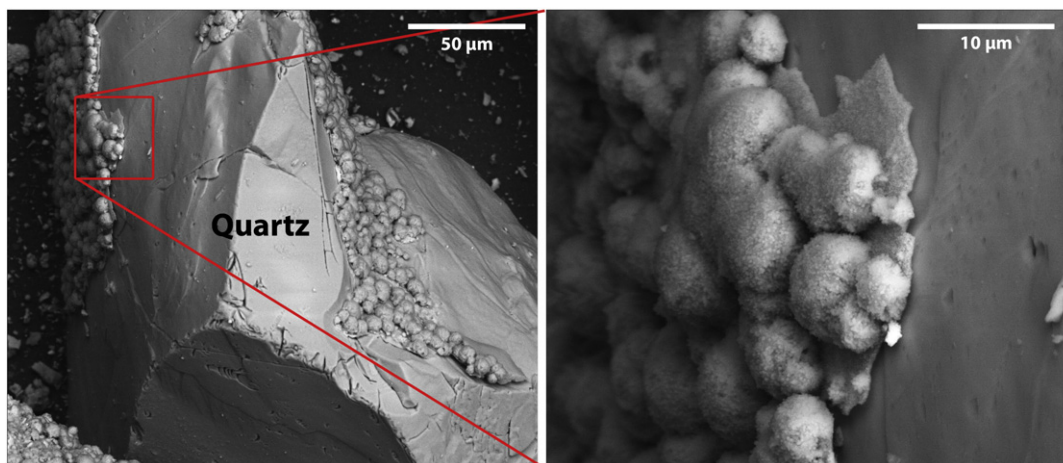


Fig. 5. BSE images of ball-shaped morphology of cancrinite forming on smoother precipitate phase on quartz grain surface.

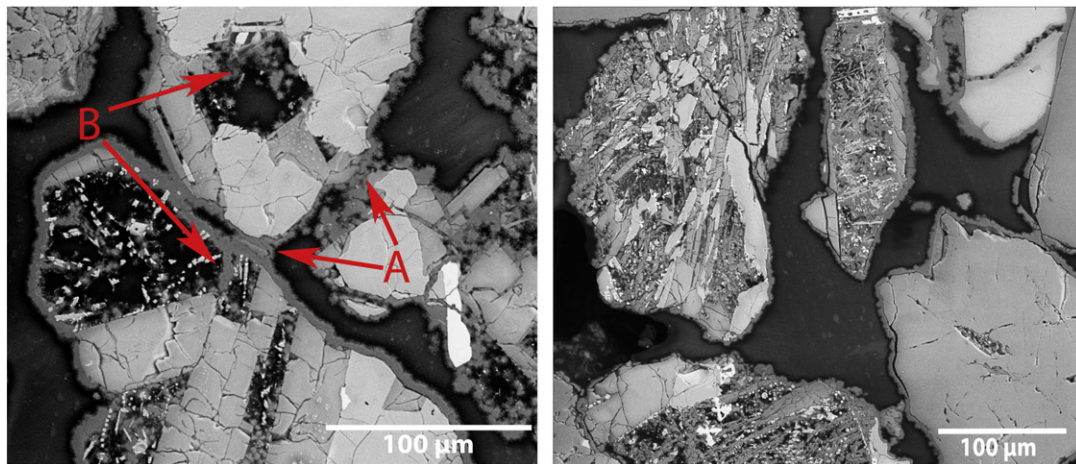


Fig. 6. BSE images of cross sections from column X showing cancrinite precipitation almost uniformly on all grain surfaces, closing off pore throats (A), and in intragranular pore space (B).

observed in the 2D SEM images of epoxied column cross-sections. During epoxy impregnation, epoxy flow between the grain surface and precipitate phase pushed the precipitates from the grain surface. Despite the increased distance, precipitates retained their original shape mimicking the grain surface. This can be seen in the right side of the right panel of Fig. 6.

3.2. Image analysis of pore space

3.2.1. Porosity reduction

Porosities determined for cross sections with precipitation present range from 0.34 to 0.37 as given in Table 1. These values are higher than those given in Cai et al. 2009. The difference is partly attributed to the lower resolution of CMT images that misses pores and throats smaller than the voxel size. More importantly, the difference is attributed to the ability in 2D SEM imaging to observe not only the intergranular porosity but also the smaller-scale intragranular porosity. The Hanford sediment grains have a high amount of intragranular porosity including fractures and cracks. This feature is a result of the geologic history of the Hanford sediments, a combination of ancient river beds and glacial and pluvial lake floods (Martin, 2010), which created complex grains consisting of basaltic lithic fragments. The imaging in this work revealed precipitation in those spaces, as shown in Fig. 6.

Also shown in Table 1 are the estimates of porosity before reaction based on the analysis of images for which precipitation

was digitally removed. These values are up to one fourth greater than the post-reaction porosities.

3.2.2. Pore and throat size distributions

The results of the erosion–dilation analysis are shown for each section composition image in Fig. 7. It is evident that precipitation causes a decrease in pore sizes. The shift of all pore sizes toward smaller pore radii is consistent with the findings from visual examinations of the images that showed uniform coating of secondary minerals. The scenario with precipitation, the blue bars, are higher at small pore radii which means that samples with precipitation present have a higher abundance of small pores. As mentioned in Section 3.1.2, small pores are created in the newly formed secondary minerals. The higher abundance of small pores in images with precipitation accounts for these newly formed small pores and the reduction in pore sizes due to precipitation. A greater number of large pores are present in the scenario with precipitation digitally removed as observed by a greater number of red bars at large pore radii. In the case where there is precipitation present, the shift in pore size to smaller pores is also noticeable by observing the distribution of medium to large pores (radius 10–200 µm). In the scenario with precipitation, the distribution of medium to large pores consists of smaller pore radii (mainly 20–90 µm radius) than for the scenario with precipitation digitally removed (radii 80–120 µm).

The observation of precipitation uniformly coating grain surfaces has a relatively uniform shift on pore size distributions, but the impact on throat size distributions is not as straightforward. Some pore throats, those that remain open with precipitation present, decrease in size while others are closed off decreasing the total number of throats. As evident in the throat size distribution for X2 in Fig. 8, there is a loss of small throats due to clogging in the scenario with precipitation present. Thus, there is a greater number of small throats in the scenario with precipitation digitally removed, red bars. However, in X3 and X4 there are a greater number of small throats with precipitation present due to the creation of additional small throats between newly formed small pores in secondary mineral precipitates and the size reduction of open throats.

Table 1

Porosities estimated before and after the reactive flow experiment. For cross sections from column X this was measured from segmented BSE composite images with precipitation and with precipitation digitally removed. For Cai et al. (2009), the values were determined by X-ray CMT imaging and 3D reconstruction of the entire column before and at the end of the experiment.

Section	Porosity after reaction	Porosity before reaction	Change in porosity
X2	0.34	0.43	0.095
X3	0.37	0.47	0.11
X4	0.37	0.44	0.068
Cai et al. (2009)	0.318	0.354	0.036

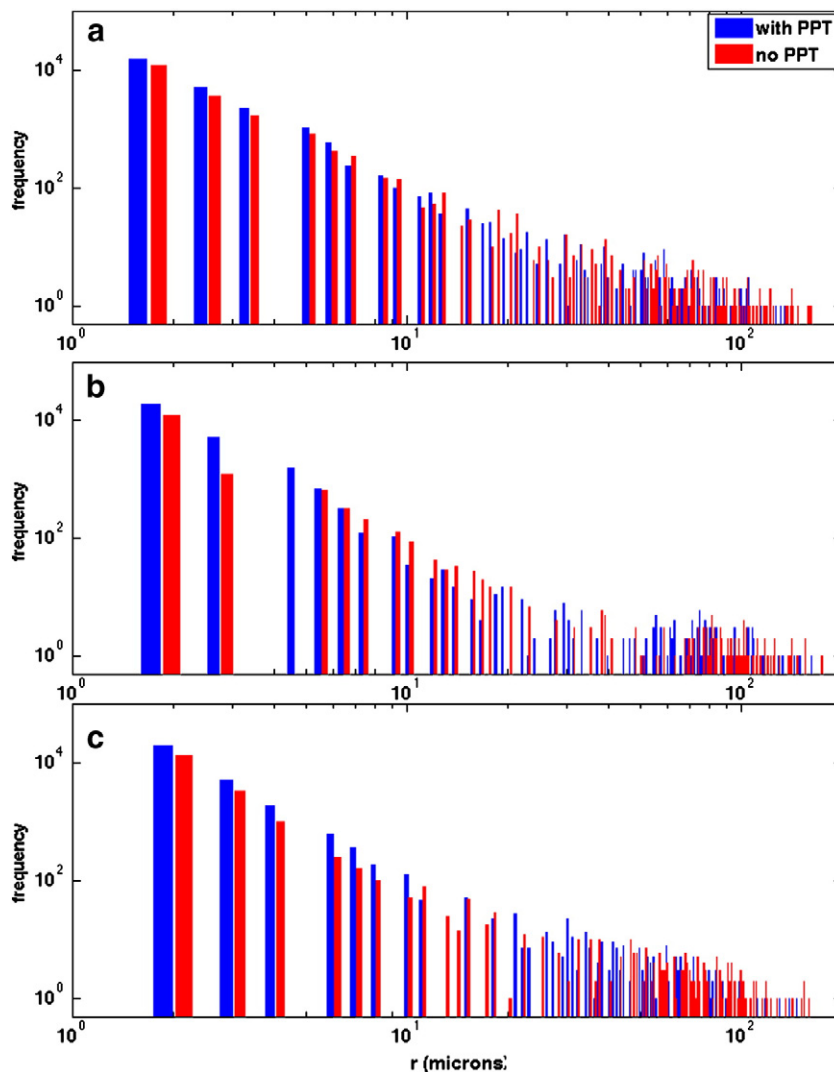


Fig. 7. Pore size distributions for cross sections (a) X2, (b) X3, and (c) X4 both with precipitation (blue) and with precipitation digitally removed (red).

In terms of the total number of pores and throats, there are a greater number of both in the scenario with precipitation present. For all three cross sections combined, the total number of pores in the scenario with precipitation present is 57,391 while it is only 38,400 with precipitation digitally removed. A total of 14,951 throats were counted with precipitation present and 13,907 throats with precipitation digitally removed. The higher abundance of pores and throats for the scenario with precipitation present is due to the large number of small pores and throats. Visual examination of BSE images reveals that these small pores and throats are part of the new pore network created within the secondary mineral precipitates. In contrast, the previous analysis of this column in Cai et al. (2009) showed a decrease in small pores and throats as the reactions progressed and the amount of precipitation increased. This difference may be attributed to the higher resolution of SEM imaging in comparison to X-ray CT imaging. Higher resolution offers the ability to observe the smaller pores that are created in secondary precipitates or

between grain-to-grain contact areas. This work also reports a higher number of total pores, up to 57,391, compared with the maximum total of 14,668 counted in Cai et al. (2009). This difference is due to the presence of intragranular pores that are visible in SEM images but undetectable in the X-ray CT images. These differences may also be due to the fact that there may have been additional precipitation in the column by the time it was sectioned for 2D imaging. There was a period of time after the reactive flow experiment and after the 3D imaging during which further reaction may have occurred.

3.2.3. Estimated permeability changes

Precipitation on grain surfaces directly reduces porosity, as described above, however the effect on permeability is much less understood. There are several relationships linking porosity to permeability, as summarized for example in Xu and Yu (2008). Many of these relationships are semi-empirical in nature and have a power law relationship between porosity and permeability. The Kozeny–Carman equation, from

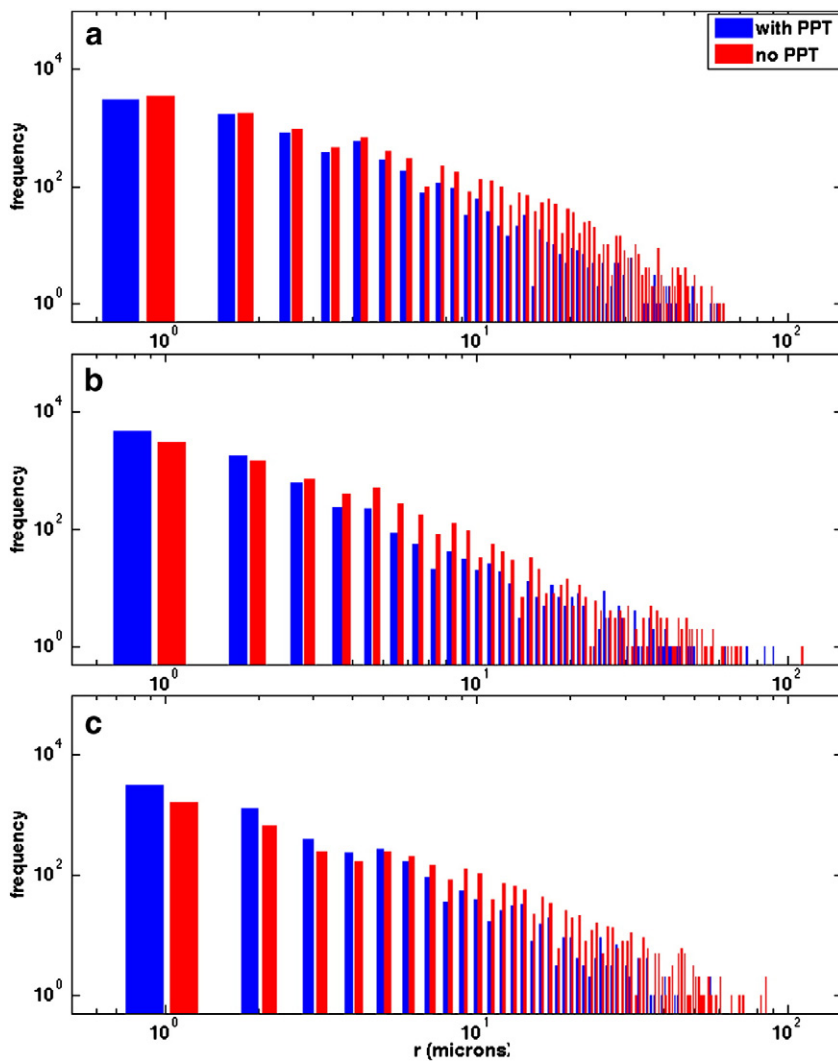


Fig. 8. Throat size distributions as determined from image erosion dilation analysis of BSE cross sections (a) X2, (b) X3, and (c) X4.

seminal work by Carman (1937) and Kozeny (1927), is widely used to estimate permeability in porous media. Here, a modified version that accounts for tortuosity was used to estimate permeability as given by,

$$K = \frac{\Phi^3 d^2}{36k(1-\Phi)^2} \quad (5)$$

where K is the permeability, Φ is the porosity, d is the mean particle diameter and k is the Kozeny–Carman constant given by $k = c\tau^2$ where c is the Kozeny constant and τ the tortuosity (Bear, 1972; Kaviani, 1995). The Kozeny constant was taken as 2.5 as in Bear (1972) for a bed packed with spherical particles. A tortuosity of 1.7 was used corresponding to the average tortuosity after reaction as determined from the 3D CT analysis of the column in Cai et al. (2009). Precipitation-induced changes in permeability, as given in Table 2, were determined based on the porosity of each section. According to these calculations, the precipitation in this experiment is expected to

decrease permeability by less than an order of magnitude. A reduction in throat sizes and the loss of flow-conducting pore throats are responsible for the reduction in permeability. While the Kozeny–Carman equation does predict a reduction in permeability, this simple relationship between porosity and permeability does not account for the effects of changes in pore throat sizes. To predict permeability accounting for changes in pore and throat sizes requires a more sophisticated approach that is beyond the scope of this work.

Table 2

Permeability as calculated using the Kozeny–Carman equation (Bear, 1972; Kaviani, 1995) from section porosities listed in Table 1.

Section	$K \text{ (m}^2\text{) with PPT}$	$K \text{ (m}^2\text{) no PPT}$
X2	2.30E – 11	6.58E – 11
X3	3.18E – 11	9.83E – 11
X4	3.29E – 11	6.86E – 11

4. Conclusions

Many new studies focus on the impact of mineral precipitation and dissolution reactions on porous media using 3D CMT imaging. This type of imaging has the ability to non-destructively image a specimen allowing for imaging both before and after reaction to track reaction-induced changes in the pore network. However, CMT imaging is currently limited in the diameter of the column that can be imaged and to a resolution on the order of microns. This work has demonstrated the capabilities of also using 2D imaging to analyze reaction-induced changes in the pore network. 2D SEM-based imaging has the advantage of high resolution and ease of mineral identification and mapping using BSE and EDS. In this work, these advantages are demonstrated by estimating porosity and pore and throat size distributions, both after and before reaction through the digital creation of a pre-precipitation scenario. The higher resolution images in this work were key to quantifying small pores and throats, pore space at grain-to-grain contacts, and intra-granular pore space.

Despite the differences between 2D SEM imaging and 3D CMT imaging, there are some network changes that are predicted using both methods. In either analysis, precipitation in the pore network caused a decrease in total porosity. 3D analysis by Cai et al. (2009) found a difference of 0.04 in total porosity while this work calculated differences ranging from 0.068 to 0.11. There are two reasons why the decrease in porosity predicted from 2D SEM analysis is larger. As mentioned above, precipitation was observed in intragranular pore regions that are not visible in 3D CMT imaging, which results in an additional decrease in porosity. Secondly, the net change in porosity calculated from the 3D analysis reflects the net mineral dissolution, which increases porosity, and subsequent precipitation. The 2D analysis accounts only for changes in porosity due to precipitation. Thus, the larger decrease in porosity observed from 2D analysis suggests that a large amount of precipitation occurs, enough to replace any pore space from mineral dissolution and an additional amount to decrease the net porosity observed in 3D. Some of this precipitation may have occurred during the extended reaction time following the final 3D CMT scan before the column was prepared for 2D image analysis.

In terms of pore and throat size distributions, there were some disagreements in the 2D SEM analysis versus the 3D CMT analysis. While the 3D CMT work in Cai et al. (2009) showed a net decrease in the total number of pores and a loss of small pores, the 2D analysis found an increase in both. The increase in small pores and the total number of pores in the 2D analysis is partly due to the creation of new small pores in the precipitates. Additionally, the observed uniform precipitate on grain surfaces decreased all pore sizes, shifting the pore size distribution to include a greater number of small pores, some of which due to resolution limitations were not observed in the 3D CMT analysis.

The other difference in 2D versus 3D observations is in the evolution of large pores. The 3D CMT analysis found a 13% increase in the number of large pores while the 2D analysis showed a decrease in large pores. Cai et al. (2009) noted that the increase in large pores was indicative of dissolution dominating in large pores. The pre-precipitation scenario

created to analyze the effect of precipitation on the pore network cannot represent changes in pore sizes due to dissolution, only precipitation. Thus in the 2D analysis, the decreases in the number of large pores results again from uniform precipitation on grain surfaces decreasing all pore sizes.

In terms of pore throats, there was a better agreement in the trends reported from both the 2D SEM and 3D CMT analyses. Both analyses found that small throats could decrease in number due to clogging and no real marked change in the number of large throats. However, opposite results were noted for the change in the total number of throats. The 3D analysis showed a decrease in the total number of throats due to throats being closed off but the 2D analysis computed an increase. The increase in the total number of throats in the 2D analysis is a result of additional small throats created between newly formed small pores in the precipitates. Additionally, in the 2D analysis, some of the pore throats actually reflect grain surface roughness. To separate the surface roughness throats from fluid conducting throats requires setting a somewhat arbitrary threshold which is beyond the scope of this work and will be examined in a future study.

The largest discrepancies between the 2D SEM analysis and 3D CMT analysis lie in the classification of small pores and throats. Many small pores and throats are in intragranular regions and thus cannot be observed in the 3D CMT images. In the bulk pore space, all pores and throats smaller than the current 3D voxel resolution of 4 μm are missed in 3D CMT images, which demonstrates one of the advantages of 2D imaging techniques. However, many small pores and intragranular pores and throats are expected to be less important in impacting permeability relative to large, connected pores. The most controlling factor for system permeability lies in changes in the flow-conducting pore throats. In this area, the two methods predicted the same trends. However, the 2D method requires setting a roughness threshold and the 3D CMT method misses small pore throats. While the precise impact of each of these factors on permeability cannot be determined using the simple porosity–permeability relationships here, we speculate that missing small pore throats in the 3D analysis would over estimate permeability. A more in depth analysis of these outcomes on permeability is beyond the scope of this work but will be determined using pore network modeling in future work.

Acknowledgments

This material is based upon work supported by the Department of Energy under Award Numbers DE-FG02-09ER64747 (SUNY Stony Brook); DE-FG02-09ER64748 (Princeton University); and KP1702030-54908 (Pacific Northwest National Laboratory). The information does not necessarily reflect the opinion or policy of the federal government and no official endorsement should be inferred. We also acknowledge the use of PRISM Imaging and Analysis Center, which is supported in part by the NSF MRSEC program through the Princeton Center for Complex Materials grant (DMR-0819860).

References

- Aharonov, E., Tenthorey, E., Scholz, C.H., 1998. Precipitation sealing and diagenesis 2. Theoretical analysis. *Journal of Geophysical Research* 103 (B10), 23969–23981.

- Algive, L., Bekri, S., Vizika, O., 2010. Pore-network modeling dedicated to the determination of the petrophysical-property changes in the presence of reactive fluid. *SPE Journal* 15 (3), 618–633.
- Barnes, M.C., Addai-Mensah, J., Gerson, A.R., 1999. The kinetics of desilication of synthetic spent bayer liquor seeded with cancrinite and cancrinite/sodalite mixed-phase crystals. *Journal of Crystal Growth* (200), 251–264.
- Bear, J., 1972. *Dynamics of Fluid in Porous Media*. Elsevier, New York.
- Bickmore, B.R., Nagy, K.L., Young, J.S., Drexler, J.W., 2001. Nitrate-cancrinite precipitation on quartz sand in simulated Hanford tank solutions. *Environmental Science and Technology* 35 (22), 4481–4486.
- Buhl, J., Stief, F., Fechtelkord, M., Gesing, T.M., Taphorn, U., Taake, C., 2000. Synthesis, X-ray diffraction, and MAS NMR characteristics of nitrate cancrinite $\text{Na}_{7.6}[\text{AlSiO}_4]_6(\text{NO}_3)_{1.6}(\text{H}_2\text{O})_2$. *Journal of Alloys and Compounds* 305, 93–102.
- Cai, R., Lindquist, W.B., Um, W., Jones, K.W., 2009. Tomographic analysis of reactive flow induced pore structure changes in column experiments. *Advances in Water Resources* 32, 1396–1403.
- Carman, P.C., 1937. Fluid flow through granular beds. *Transactions of the Institute of Chemical Engineers* 15, 150–167.
- Chang, H.S., Um, W., Rod, K., Serne, R.J., Thompson, A., Perdrial, N., Steefel, C.I., Chorover, J., 2011. Strontium and cesium release mechanisms during unsaturated flow through waste-weathered Hanford sediments. *Environmental Science and Technology* 45 (19), 8313–8320.
- Chorover, J., Choi, S., Amistadi, M.K., Karthikeyan, K.G., Crosson, G., Mueller, K.T., 2003. Linking cesium and strontium uptake to kaolinite weathering in simulated tank waste leachate. *Environmental Science and Technology* 37, 2200–2208.
- Colon, C.F.J., Oelkers, E.H., Schott, J., 2004. Experimental investigation of the effect of dissolution on sandstone permeability, porosity, and reactive surface area. *Geochimica et Cosmochimica Acta* 68 (4), 805–817.
- Crosson, G.S., Choi, S.Y., Chorover, J., Amistadi, M.K., O'Day, P.A., Mueller, K.T., 2006. Solid-state NMR identification and quantification of newly formed aluminosilicate phases in weathered kaolinite systems. *The Journal of Physical Chemistry. B* 110 (2), 723–732.
- Deng, Y., Harsh, J.B., Flury, M., Young, J.S., Boyle, J.S., 2006. Mineral formation during simulated leaks of Hanford waste tanks. *Applied Geochemistry* (21), 1392–1409.
- Doyen, P.M., 1988. Permeability, conductivity, and pore geometry of sandstone. *Journal of Geophysical Research* 93 (B7), 7729–7740.
- Ehrlich, R., Kennedy, S.K., Crabtree, S.J., Cannon, R.L., 1984. Petrographic image analysis. I. Analysis of reservoir pore complexes. *Journal of Sedimentary Petrology* 54 (4), 1365–1378.
- Emmanuel, S., Berkowitz, B., 2005. Mixing-induced precipitation and porosity evolution in porous media. *Advances in Water Resources* 28, 337–344.
- Emmanuel, S., Berkowitz, B., 2007. Effects of pore-size controlled solubility on reactive transport in heterogeneous rock. *Geophysical Research Letters* 34.
- Emmanuel, S., Ague, J.J., Walderhaug, O., 2010. Interfacial energy effects and the evolution of pore size distributions during quartz precipitation in sandstone. *Geochimica et Cosmochimica Acta* 74, 3539–3552.
- Gouze, P., Hassani, R., Bernard, D., Coudrain-Ribstein, A., 2001. Computing permeability change in sedimentary reservoirs including clays: application to the Bray fault zone (Paris Basin). *Bulletin de la Societe Geologique de France* 172 (4), 427–436.
- Kaplan, D.I., Serne, R.J., Parker, K.E., Kutnyakov, I.V., 2000. Iodide sorption to subsurface sediments and illitic minerals. *Environmental Science and Technology* 34, 399–405.
- Kaviany, M., 1995. *Principles of Heat Transfer in Porous Media*. Springer, New York.
- Kozeny, J., 1927. Ueber kapillare Leitung des Wassers im Boden. *Sitzungsberichte Akademie der Wissenschaften in Wien* 136, 271–306.
- Lasaga, A.C., 1998. *Kinetic Theory in the Earth Sciences*. Princeton University Press, Princeton, New Jersey.
- Liu, C., Zachara, J.M., Qafoku, O., Smith, S.C., 2003. Effect of temperature on Cs^+ sorption and desorption in subsurface sediments at the Hanford Site, U.S.A. *Environmental Science and Technology* 37, 2640–2645.
- Martin, C.J., 2010. Overview of Hanford hydrogeology. In: DOE (Ed.), *Hanford Site Groundwater Monitoring and Performance Report for 2009*, Richland, WA.
- McKinley, J.P., Zeissler, C.J., Zachara, J.M., Serne, R.J., Lindstrom, R.M., Schaef, H.T., Orr, R.D., 2001. Distribution and retention of ^{137}Cs in sediments at the Hanford Site, Washington. *Environmental Science and Technology* 35, 3433–3441.
- Mon, J., Deng, Y., Flury, M., Harsh, J.B., 2005. Cesium incorporation and diffusion in cancrinite, sodalite, zeolite, and allophane. *Microporous and Mesoporous Materials* 86, 277–286.
- Qafoku, N.P., Ainsworth, C.C., Szecsody, J.E., Bish, D.L., Young, J.S., McCready, D.E., Qafoku, O.S., 2003. Aluminum effect on dissolution and precipitation under hyperalkaline conditions: II. Solid phase transformations. *Journal of Environmental Quality* 32, 2364–2372.
- Rijniers, L.A., Huinink, H.P., Pel, L., Kopinga, K., 2005. Experimental evidence of crystallization pressure inside porous media. *Physical Review Letters* 94.
- Rod, K.A., Um, W., Flury, M., 2010. Transport of strontium and cesium in simulated Hanford tank waste leachate through quartz sand under saturated and unsaturated flow. *Environmental Science and Technology* 44 (21), 8089–8094.
- Scherer, G.W., 2004. Stress from crystallization of salt. *Cement and Concrete Research* 34, 1613–1624.
- Tenthorey, E., Scholz, C.H., 2002. Mapping secondary mineral formation in porous media using heavy metal tracers. *Journal of Geophysical Research* 107 (B10).
- Um, W., Serne, R.J., Yabusaki, S.B., Owen, A.T., 2005. Enhanced Radionuclide immobilization and flow path modifications by dissolution and secondary precipitates. *Journal of Environmental Quality* 34, 1404–1414.
- Van Marcke, P., Verleye, B., Carmeliet, J., Roose, D., Swennen, R., 2010. An improved pore network model for the computation of the saturated permeability of porous rock. *Transport in Porous Media* (85), 451–476.
- Vogel, H.-J., Roth, K., 2001. Quantitative morphology and network representation of soil pore structure. *Advances in Water Resources* 24, 233–242.
- Weibel, E.R., 1979. *Stereological Methods*. Academic Press, London.
- Xu, P., Yu, B., 2008. Developing a new form of permeability and Kozeny–Carman constant for homogenous porous media by means of fractal geometry. *Advances in Water Resources* 31, 74–81.
- Zachara, J.M., Smith, S.C., Liu, C., McKinley, J.P., Serne, R.J., Gassman, P.L., 2002. Sorption of Cs^+ to micaceous subsurface sediments from the Hanford site, USA. *Geochimica et Cosmochimica Acta* 66 (2), 193–211.